Sensorless Control of a Hub Mounted Switched Reluctance Motor

A. B. Kjaer, A. D. Krogsdal, E. H. Nielsen, F. M. Nielsen, S. Korsgaard, S. P. Moeller

Department of Materials and Production, Aalborg University
Fibigerstraede 16, DK-9220 Aalborg East, Denmark
Email: fmni13@student.aau.dk,
Web page: http://www.mechman.m-tech.aau.dk/

Abstract
This paper covers sensorless control by the use of a flux linkage/current method, applied on a single phase double U-core switched reluctance machine (SRM). This problem is stated by Johnson Controls, that has shown interest in this type of motor and control strategy for an Ultra Short Axial Compressor (USAC). The SRM technology concept is briefly described, and a dynamic model of the system is derived. The dynamic simulation model of the SRM system takes inputs from three finite element analysis (FEA) look-up tables, which describes the magnetisation curves, torque and core loss characteristics of the SRM prototype. The SRM is operated through an inverter, which is connected to a digital signal processor (DSP) through an interface board. This board and inverter used for communication of the SRM are designed for this specific motor. The motor is initially tested with a standard feedback control method with position and speed feedback from a Hall sensor, where controllers for speed and current control are designed. Sensorless estimation of position and speed is developed for the SRM prototype based on flux linkage and current FEA. Testing yielded reasonable results with regards to speed estimation, but showed a 20 % error in the position estimation. The sensorless feedback was not used for closed loop control.

Keywords: Sensorless Control, Switched Reluctance Motor, Double U-core, Inverter, Multi Stage Cooling System

1. Introduction

The motivation for studying sensorless control of a hub mounted single phase double U-core SRM is, that Johnson Controls has patented a multi stage cooling system with five SRMs called a USAC, where some problems arise with respect to position feedback due to a harsh environment of operation. This system differs from the system that Johnson Controls has used in the past, since that system had an external induction motor, which drove seven impellers. However, for environmental reasons this system was redesigned in order to avoid the use of toxic refrigerants, and instead utilise water. By introducing these hub mounted SRMs, problems arise as encoders or Hall sensor are not suitable for the operation environment of the USAC, and this leads to the interest in applying sensorless control.

The working principle of an SRM is utilisation of the fact that the rotor always moves towards the positions with the least reluctance, and thereby the highest inductance, when a current is induced in the coils [1], and this relation is described in equation (1).

$$L = \frac{N^2}{\mathcal{R}} \tag{1}$$

Here, L is the inductance, $\mathcal{R}$ is the reluctance, and N is the number of windings in each coil. The SRM utilises the double U-core technology, where the flux path is shorter than for classic types of SRMs. This short flux path is illustrated in Fig. 1, and the U-core development is described and patented in [2].

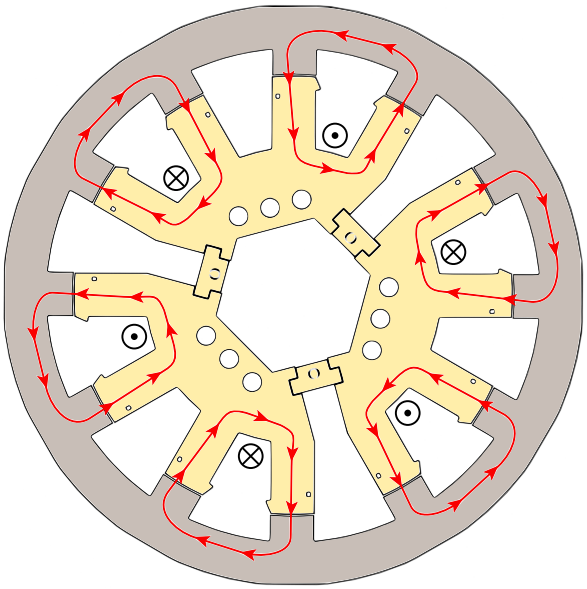

Fig. 1 Illustration of the SRM and U-core technology. Grey part is the rotor, while the yellow part is the stator. The red arrows show the flux paths.

The double U-core is developed and described in [3]. The main advantages for implementing the double U-core SRM are:

- No permanent magnets are needed, which reduces costs and is more environmentally sound [4].
- Shorter flux path, which decreases the core losses and thereby increases the efficiency.
- Single phase motor which makes it easier to control.
- Since windings are only present on the stator, there are no copper losses on the rotor.

The main focus of this paper is to investigate the possibility of using sensorless position estimation, to control the SRM. The final design of the SRM was given from the project start as well as the FEA look-up tables. An exploded view of the SRM can be seen in Fig. 2.

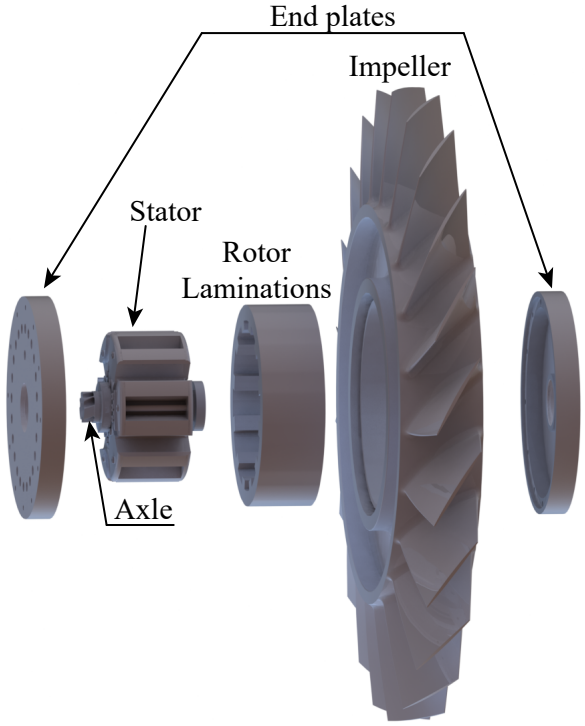

Fig. 2 Exploded view of the SRM, where the main components are presented.

2. Dynamic Model

To simulate the dynamic response of the SRM, a nonlinear model is derived. An overview of the model is seen in Fig. 4 The voltage equation is derived from Kirchhoff's Voltage Law, and Newtons II Law for rotational motion is used to establish the mechanical model.

The voltage drop in the electrical system is expressed in equation 2. This equation contains a resistance voltage drop, an inductance voltage drop and a voltage drop due to the back-emf. However, as this equation includes the derivatives of the inductance as a function of the rotor position, the inductance must be known for all rotor positions. Therefore, FEA look-up tables are utilised as these provide an approximation of the inductance as a function of the current and rotor position. Index i denotes the considered coil.

$$u_i = R_i(T)\, i_i + L_i \frac{di_i}{dt} + \frac{\partial L_i}{\partial \theta} \frac{\partial \theta}{dt}\, i_i \tag{2}$$

These FEA look-up tables describe the magnetisation characteristics, i.e. the flux linkage of the SRM and the torque as a function of the rotor position θ, and current i_i. The output from the FEA look-up tables are interconnected, and this can be seen in Fig. 3.

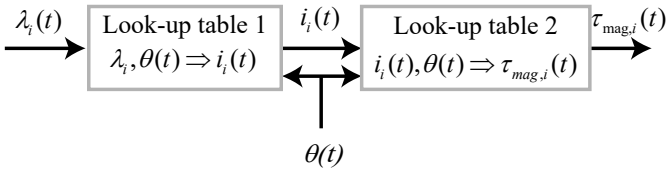

Fig. 3 Interconnection between the look-up tables.

Here, the first look-up table for the magnetisation characteristics must have a flux linkage and rotor position as input. The flux linkage is derived from the voltage equation described in equation (3). The first look-up table thereby supplies a current to the second look-up table, which outputs the torque to the simulation model.

$$\begin{aligned} u_i &= R_i(T)\, i_i + \frac{d\lambda_i}{dt} \Rightarrow \\ \lambda_i &= \int u_i - R_i(T)\, i_i\, dt \end{aligned} \tag{3}$$

Here, u_i is the applied voltage, i_i is the current in each coil of the motor, λ_i is the flux linkage, and $R_i(T)$ is the coil resistance. The core loss inside the SRM is also calculated from a FEA look-up table. Copper losses are also included by considering the resistance of the coils. Mechanical losses are modelled, and the implementation of all these losses are described in [5]. The connection of the mechanical model and the FEA look-up tables can be seen in Fig. 4.

The describing equations are given in equation (4) and (5).

$$J_r\, \ddot{\theta} = \sum \tau \tag{4}$$

$$J_r\, \ddot{\theta} = \tau_{mag} - \tau_c - \tau_v - \tau_{core} - \tau_L \tag{5}$$

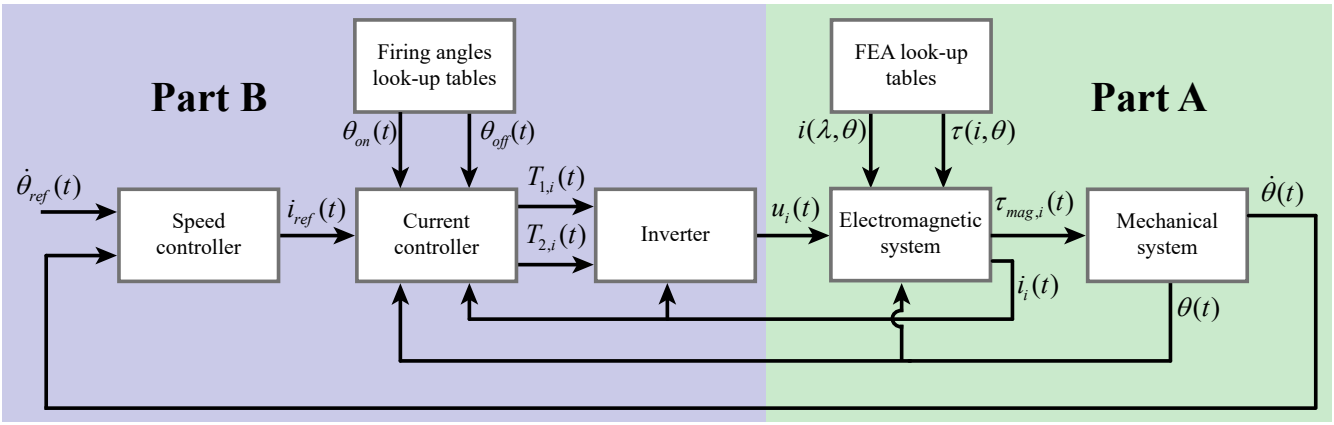

Fig. 4 Overview of the dynamic simulation model.

Where τ is the output torque, J_r is the mass moment of inertia of the SRM, and τ_L is the counteracting torque produced by the impeller. Here, it can be seen that the mechanical system receives the torque and the core loss as input from the look-up tables, and the rotor speed and position are fed back to the look-up tables in order to determine a current.

Before the FEA look-up tables were implemented in the dynamic model, they were verified in the test setup, and the tables were corrected in order to represent the test setup most sufficiently.

3. Verification of FEA Look-up Tables

The FEA makes it possible to model the positions between the aligned and unaligned position of the rotor, which is advantageous in order to obtain a more reliable simulation model. The FEA model of the magnetisation curves is therefore verified by measuring inductance in aligned and unaligned positions. The results are shown in Fig. 5. The lines for the measured inductance is the mean value that was measured, while the two other lines represents the FEA generated magnetisation curves.

Here, the maximum deviation of the FEA compared to the measured inductance for the aligned position in Fig. 5 is 5.9 %, and for the unaligned position the deviation is 38.5 %. This large deviation of the FEA compared to the inductance for the unaligned position is caused by 3D effects. These effects are not modelled in the FEA, as this model is based on a 2D static FEA. The 3D effects appears as out-of-plane flux linkage, where the flux path is shorter through the end material than through the air gap to the poles; hence, this introduces large deviation of inductance in the unaligned position.

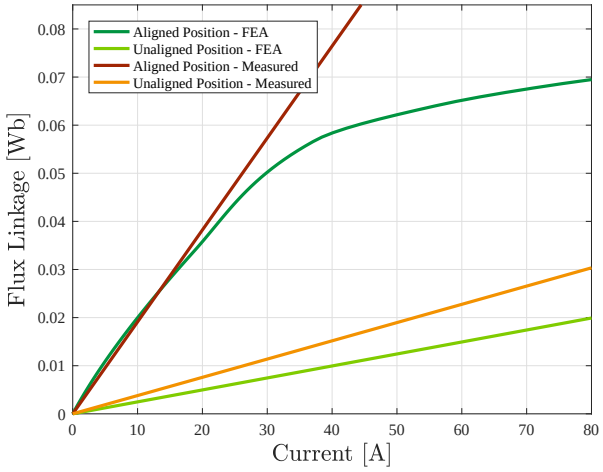

Fig. 5 Verification of the FEA in the aligned and unaligned position for the SRM.

4. Correction of FEA Look-up Tables

Due to the large deviation of inductance in the FEA compared to the experimental data, the FEA look-up tables are corrected. The large deviation of the inductance in the unaligned position will, if not corrected, results in a lower inductance in the dynamic model, which gives a lower torque and thereby deviations in the verification of the simulation model. A method to correct the look-up tables is presented in [3], by considering the ratio of energy of the experimental data and the FEA data for the unaligned position. For these calculations it is assumed, that the aligned inductance is the same for the FEA and the experimental data. Equation (6) is utilised to calculate the energy ratio $W_{3D,2D}$.

$$W_{3D,2D} = \frac{W_{3D}}{W_{2D}} = \frac{\frac{\lambda^2}{2L_{u,3D}} - \frac{\lambda^2}{2L_a}}{\frac{\lambda^2}{2L_{u,2D}} - \frac{\lambda^2}{2L_a}} = \frac{L_a \Psi_{3D,2D} - L_{u,2D}}{L_a - L_{u,2D}} \tag{6}$$

Here, the index *3D*, is used for the experimental data measured in the test setup, while *2D* is used for the FEA data. L_a is the designation of the aligned inductance, and L_u is the designation for the unaligned inductance and λ is the flux linkage. The current look-up table is corrected by equation (7).

$$i_{3D}(\theta_i, \lambda) = i_a(\lambda) + W_{3D,2D}(i_{2D}(\theta_i, \lambda) - i_a(\lambda)) \quad (7)$$

This equation only corrects the unaligned inductance, since this is dependent of rotor position. Thus, for the aligned position of the rotor the inductance follows the magnetisation curve. This is shown in Fig. 6, where the blue curves represent the corrected FEA magnetisation curves. The original FEA data is denoted by i_{2D}, while i_{3D} is the corrected current simulation data.

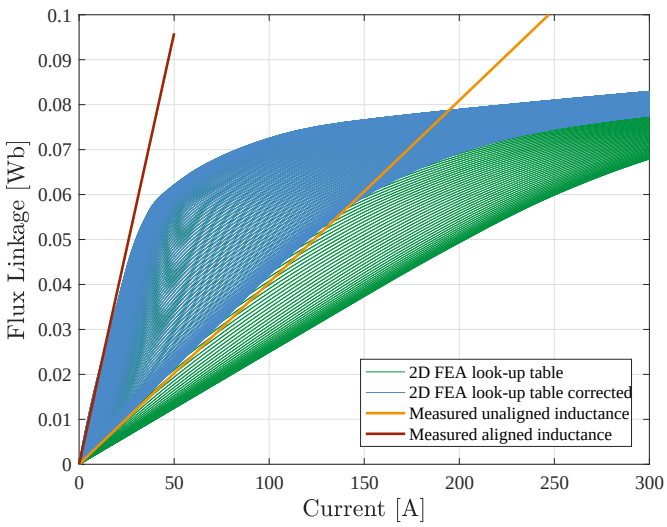

Fig. 6 Blue curves show the corrected magnetisation curves, while the green curves represent the original data.

It is important that the torque curves have the same change of energy as for the corrected magnetisation curves. Hence, the torque curves are corrected, such that the energy level is the same for the FEA look-up tables. The method for this correction is described in greater detail in [3].

5. Linearisation

The nonlinear model of the system is linearised, such that linear control theory can be applied, and controllers for the system can be designed, since controllers for the speed and current are desired. Part A on Fig. 4 is the part of the nonlinear model, which has been linearised, as these contains nonlinear terms. The expanded governing voltage equation for the electrical part of the motor is shown in equation (8).

$$u_i = R_i(T)\, i_i + \frac{\partial \lambda_i(\theta, i_i)}{\partial i_i}\frac{di_i}{dt} + \frac{\partial \lambda_i(\theta, i_i)}{\partial \theta}\frac{d\theta}{dt} \quad (8)$$

From magnetisation curves, it is evident that the terms $\frac{\partial \lambda_i(\theta, i_i)}{\partial i_i}$ and $\frac{\partial \lambda_i(\theta, i_i)}{\partial \theta}$ are nonlinear. Therefore, a linearisation of these partial derivatives have been performed. For research purposes two linearisation working ranges are made. Working range 1 represents the test system in the laboratory with a smaller DC supply, and working range 2 is for higher currents. Working range 2 is not considered. The linear current region for the small DC supply is calculated between 0-20 A and between the angles 4°-11°. The partial derivative of the flux linkage with respect to the rotor position and current yields the inductance, and therefore an average inductance L_{lin} is calculated in the linear region shown in Fig. 7. The red lines represent the region, which is linearised. In Fig. 8 the linear region for the flux linkage with respect to the rotor position is illustrated, and an average gradient K_λ is calculated.

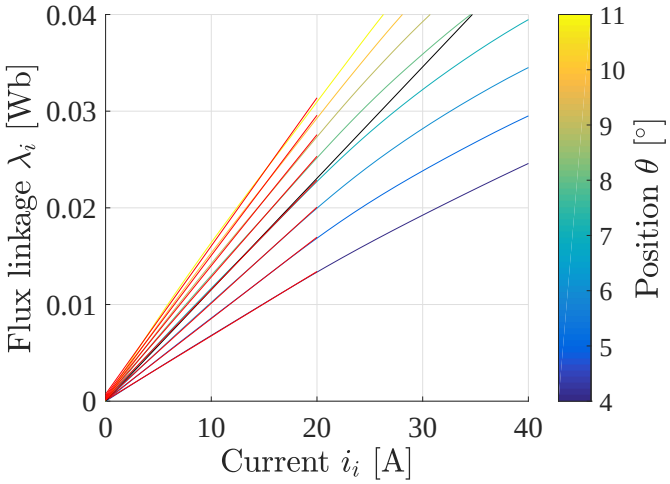

Fig. 7 Linearisation of inductance L_{lin} in working range 1.

The nonlinear back-emf is replaced by the term K_λ, and the linearised voltage equation is presented in equation (9).

$$u_i = R_i(T)\, i_i + L_{lin}\frac{di_i}{dt} + K_\lambda \frac{d\theta}{dt} \quad (9)$$

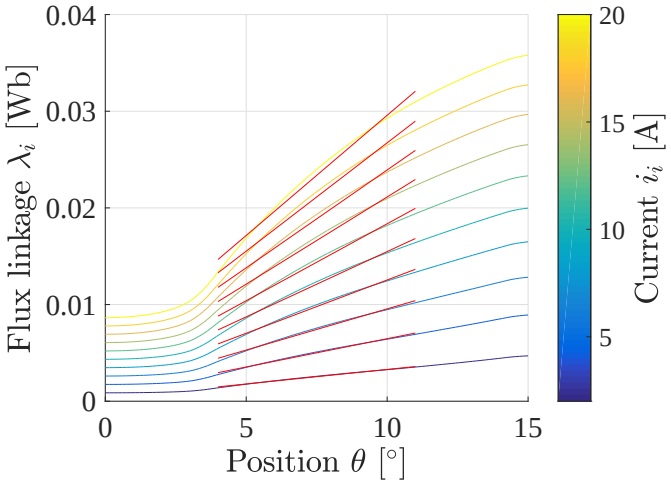

Fig. 8 Linearisation of flux linkage with respect to rotor position in working range 1.

The mechanical system has also been linearised as this also has some nonlinearities. For instance the Coulomb friction, windage, and core losses are neglected. A linear expression for τ_{mag} is found, and the linearised equation for the mechanical system is shown in equation (10).

$$J_r \frac{d\omega}{dt} = K_\lambda \, i_i - B_v \, \omega \tag{10}$$

Equation (9) and (10) are Laplace transformed with initial conditions set to zero. The final linear block diagram is presented in Fig. 9.

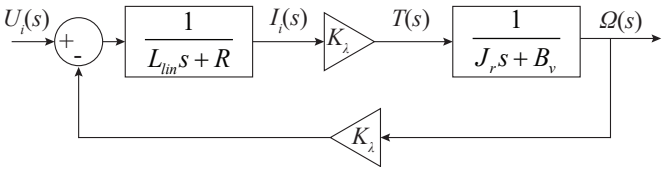

Fig. 9 Linear block diagram representation of the SRM [6, p. 120].

6. Controller Design

Controllers have been designed for the rotor speed and the current, and these gives input to the nonlinear model as shown in Fig. 4. These are necessary, because the SRM is not controlled by a frequency converter, but by an inverter, where the duty cycle is varied in order to obtain the desired speed and torque. The variable duty cycle, that determines when to conduct current through the coils in the SRM, is calculated by the current controller, which receives a reference current from the speed controller. Both of these controllers are PI controllers and presented in [5].

The implementation of the PI current controller with anti-windup is illustrated in Fig. 10.

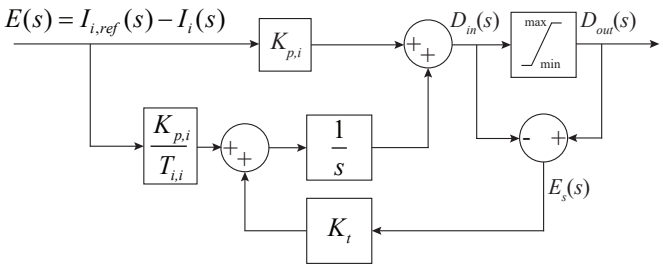

Fig. 10 Anti-windup implemented on the integral term of the PI current controller.

Here, the controller receives the error of the reference current $I_{i,ref}(s)$ with respect to the measured current $I_i(s)$. This error is gained with an integral constant $\frac{K_{p,i}}{T_{i,i}}$, and a proportional gain $K_{p,i}$. The anti-windup prevents the controller from accumulating a large error. The output from the controller is the duty cycle, and the saturation limits for the signal output is therefore set to be between 0 and 1. The effect of the current controller is tested in the linear model, then tested in the nonlinear model, and finally on the test setup. The linear and nonlinear model are compared by utilisation of the current controller with a reference at 10 A. This comparison is shown in Fig. 11.

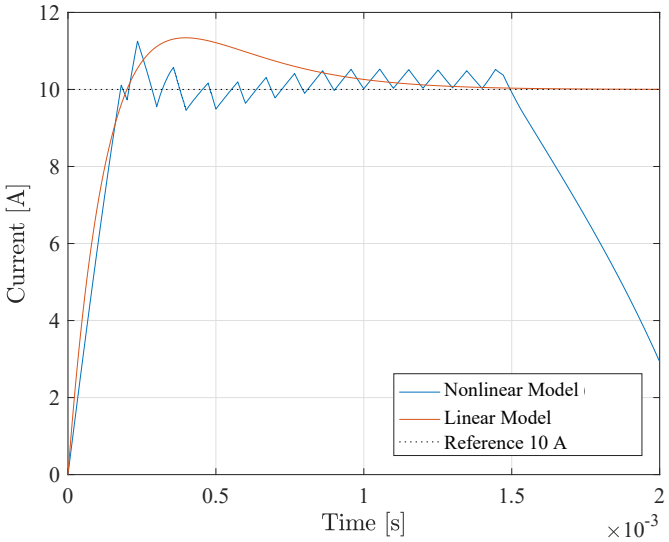

Fig. 11 Comparison of the nonlinear and linear model at a speed of 1600 rpm.

From this figure it is evident, that the linear model simulates the dynamic behaviour of the nonlinear model and settles at a steady state value around 10 A. The effect of the current controller is verified in the nonlinear model, and is therefore implemented in the test setup. The test results for the current controller are shown in Fig. 12.

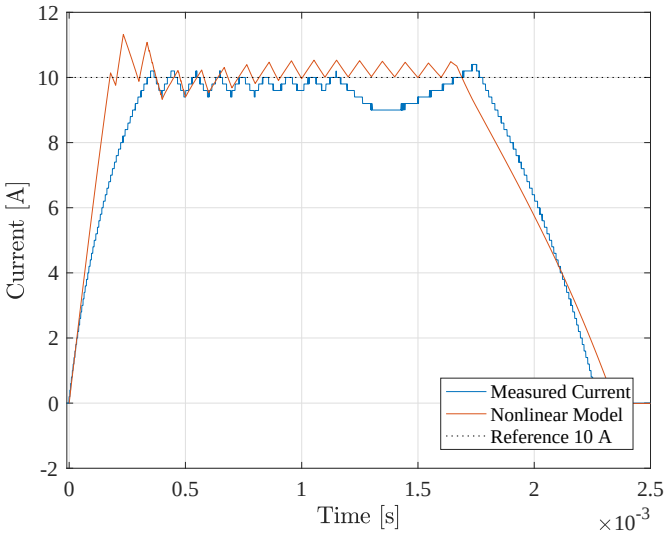

Fig. 12 Comparison of the nonlinear and test setup at a speed of 1600 rpm, with a current reference at 10 A.

Here, it is clear that the nonlinear model emulates the dynamic response of the test setup as well. However, the current build up is faster in the nonlinear model, which is explained by a small offset of the commutation angle. This offset results in larger inductance in the test setup, and thereby a slower current build up. However, it is chosen that the nonlinear model represents the test setup sufficiently to implement sensorless control, which requires that a current reference can be obtained.

7. Sensorless Control

The term sensorless refers to the use of other means to gain feedback from the system, rather than using sensors directly on the output that is to be controlled. In this case, the rotor speed and positions are desired, and electrical feedbacks from current transducers are used. This feedback is also used for the current controller, and is measured at the supply lines to the coils in the SRM. The implementation of sensorless control might cause inaccuracies in the position measurement. However, it has some advantages, which are:

- Reduction of cost.
- No need for a positioning sensor (e.g. Hall sensor, encoder).
- Motor can operate in harsh environments.
- No extra mounting arrangement.

For the USAC application from Johnson Controls, this control method is a necessity, because it is not possible to mount a position sensor on each of the SRMs. The sensorless control method which has been tested on the SRM prototype is the flux/current method. This method is presented in [7]. based on an estimate of the flux linkage, measurement of current in the coils and FEA simulations of the magnetisation in the SRM.

The principle of this method is shown in Fig. 13.

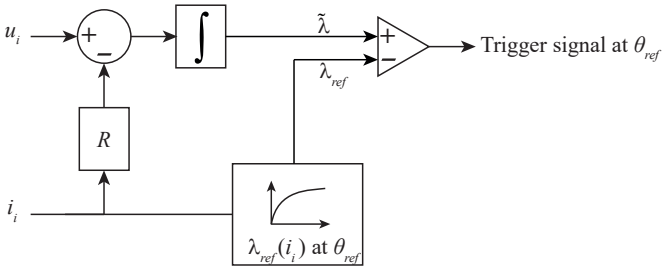

Fig. 13 Block diagram of the sensorless control method [7].

The block, which outputs λ_{ref}, is the FEA magnetisation look-up table. This look-up table estimates the flux-linkage from the measured current in the coils in the SRM. This current is also utilised in the voltage equation to calculate the theoretical flux linkage. This estimated flux linkage is denoted as $\tilde{\lambda}$ and derived from the integral in equation (11).

$$\tilde{\lambda} = \int_t (u_i - R_i(T) i_i) dt \tag{11}$$

The right part of the block diagram in Fig. 13 tracks the reference with respect to the output from the look-up table. When the estimated flux linkage $\tilde{\lambda}$ becomes larger than λ_{ref}, a trigger signal is generated, and this position of the rotor is called θ_{ref}. This trigger signal is then used to estimate the speed of the rotor. The time between this trigger signal and the next trigger signal is determined, and used in equation (12).

$$\omega = \frac{\theta_{stroke}}{t_{trig,2} - t_{trig,1}} \tag{12}$$

The stroke angle for the SRM is 30°, and thereby the angular velocity can be approximated. However, due to the fact that there is no position feedback, the only way to determine when to commutate the coils in the SRM, is by measuring the time from the trigger signal is given and until the rotor returns to an unaligned position. This trigger signal is for this control method generated at a specific angle of the rotor, which has to be chosen carefully. This is illustrated in Fig. 14.

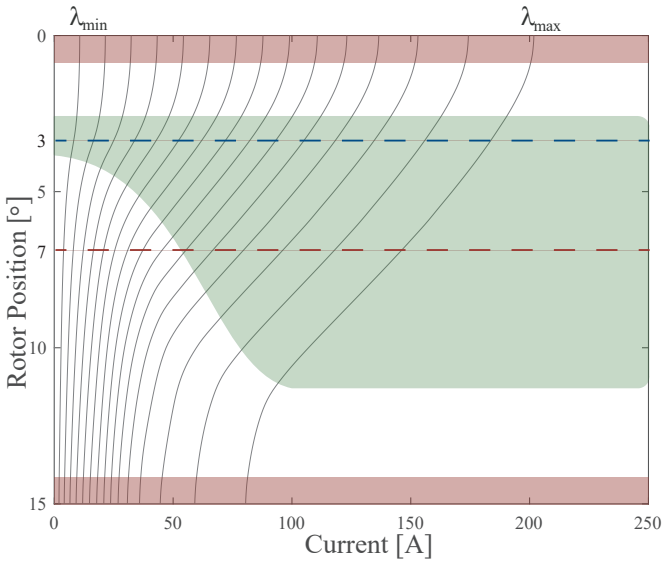

Fig. 14 Determination of the triggering angle for the sensorless control.

Here, it can be seen that in the range of 3.5-7° is the optimal position for a trigger signal. This is due to the fact that current gradients at small currents are almost infinite. A trigger signal is thereby chosen to be sent at 7°, because the integration, expressed in equation (11), can be evaluated for a longer period of time. By choosing 7° as the trigger signal position, the expected number of samples dependent of the rotor speed can be seen in Fig. 15. Here, it is also seen, that it is only possible to achieve around 5 samples during one integration period for a rotor speed of 2500 rpm, utilising this sensorless control method. Therefore it is decisive that this method is not used for rotor speed above 2500 rpm.

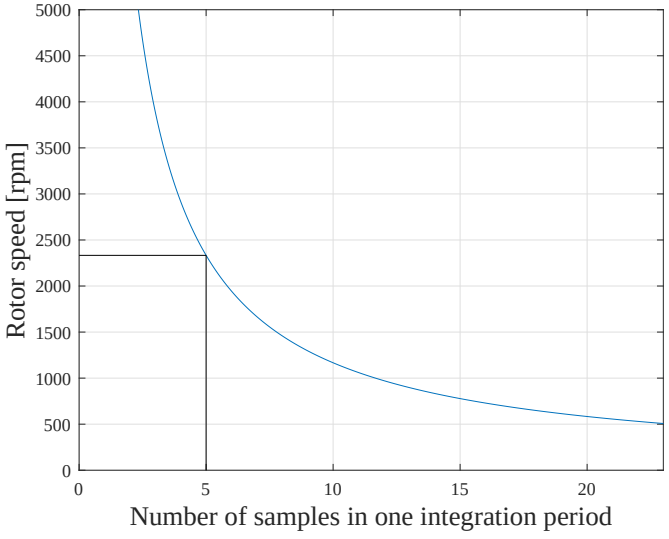

Fig. 15 The figure shows the influence of the rotor speed on the number of samples during one integration period.

Before implementing the sensorless control strategy into the test setup, it was implemented in the nonlinear model, in order to test its performance. In Fig. 16a, the simulated position and the estimated position are shown, and in Fig. 16b the corresponding current response is shown. The reference rotor speed is set to 1400 rpm and the commutation angles are $\theta_{on} = 0°$, while $\theta_{off} = 13°$. Here, the position deviation was found to be 0.23 %, which is acceptable for utilising in the USAC if running below 2500 rpm. However, due to limitations in the implementation in the test setup, such accuracy cannot be expected here.

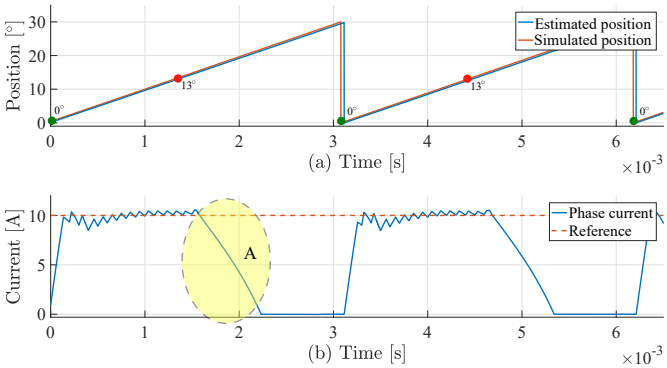

Fig. 16 (a) Estimated and simulated rotor position. (b) Corresponding current.

It should be noticed that braking torque is generated due to current flowing in each coil, when aligned position is passed. This is shown in area A in Fig. 16b.

8. Design of Interface Board

An interface board is developed. The purpose of this interface board is to operate as a communication circuit between the DSP and the inverter, and also facilitate hardware safety in case of overcurrent in the SRM coils, or an emergency stop button is pushed. This safety is ensured by using a comparator chip, an AND-logic chip, and a CMOS Latch. With the use of optical transmitters and receivers the board ensures galvanic isolation between the high voltage side on the inverter and the low voltage side in the DSP. The interface board also acquires data of the current via transducers in each of the coils. The data is used for the current controller implemented in the DSP.

9. Implementation in the DSP

A program is written in C to control the SRM, and to collect feedback signals from the current transducers by use of a DSP. Problems arise as the DSP has limited memory, and computational heavy operations

such as integration and function evaluation results in stack overflow. As the sensorless method depends on the ability to calculate the flux linkage, an integration scheme using arithmetic operations is needed. This is done by using a trapezoidal integration scheme that has a degree of precision of 1. The scheme approximates the area under the function to be integrated, by summing trapezoidal panels, as shown in equation (13) [8].

$$J = \int_b^a f(x)\,dx \approx \frac{b-a}{n}[\tfrac{1}{2}f(a) + f(x_1) + f(x_2) + \cdots + f(x_{n-1} + \tfrac{1}{2}f(b)] \quad (13)$$

The trapezoidal integration is implemented in the DSP, and it is used to estimate the flux linkage $\tilde{\lambda}$ from the current and voltage measurements in the coils. To test the flux/current method, the magnetisation curve at the chosen reference angle at 7° has to be implemented in the DSP. Here, two arrays containing discrete data of flux linkage and current within the chosen working range are inserted and used to estimate the chosen reference angle θ_{ref}. A while loop is utilised to compare the measured current with the discrete reference currents. The while loop runs until the measured current is either greater than or equal to a value in the current array. The corresponding entry in the flux linkage array is afterwards compared with the estimated flux linkage $\tilde{\lambda}$ in an if-statement, and if $\tilde{\lambda}$ is greater than the reference flux linkage λ_{ref}, a trigger signal is generated, and the integral is reset. In the test setup, feedback control is not utilised; hence, the trigger signals are not used to estimate a velocity, but rather to estimate a position, which can be compared with results from a Hall sensor. In order to simplify the test, the SRM is commutated in 0° and 15°. To verify the position estimation of the sensorless control method, a pin is toggled every time the motor is in 0°, and when the estimated flux linkage $\tilde{\lambda}$ exceeds the reference flux linkage λ_{ref}. The utilised Hall sensor consists of 24 magnets, where the rotor position is known only for every 15°. Hence, a position estimate for the Hall sensor is introduced, under the assumption that the motor rotates with a constant speed as stated in equation (14).

$$t_{hall} = \frac{\theta(\frac{\pi}{180})}{\omega} \quad (14)$$

Here, θ equals the 7°, ω is the speed estimated with the Hall sensors, and t_{hall} is the estimated time it will take the SRM to reach the reference angle θ_{ref}. The tests are conducted with a current reference of 10 A, a DC voltage of 30 V, and a steady state speed at 1560 rpm. The test result of the sensorless control is shown in Fig. 17.

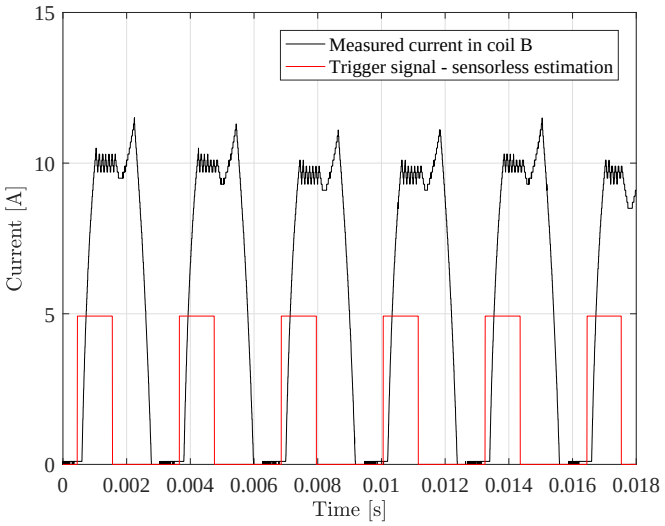

Fig. 17 Test results of the sensorless control.

As shown in the figure, the sensorless position estimation is quite constant, where no significant deviation during different current build ups are present. A comparison between the the sensorless and Hall sensor position estimation is shown in Fig. 18. As shown in Fig. 18, a deviation between the hall sensor and the sensorless control is present. Here, the sensorless control method triggers at 10°, where the Hall sensors triggers at 7°, hence the sensorless method overestimates the position by 3°. From the test data it is evident, that the

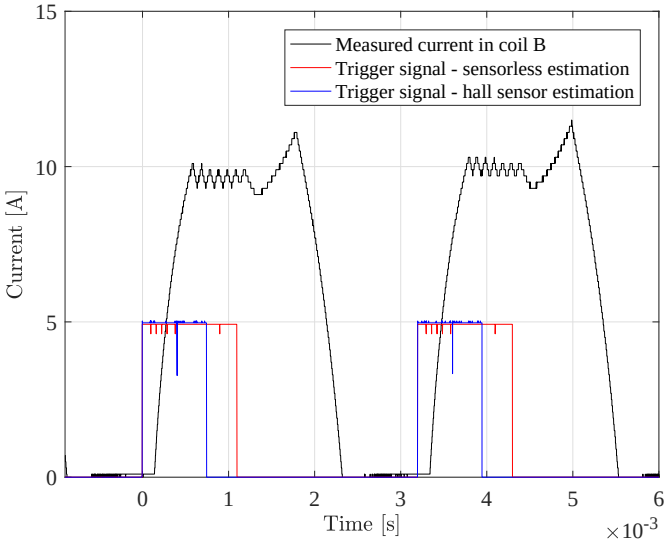

Fig. 18 Comparison between the position estimation with the sensorless control method (red) and the hall sensors (blue) [5].

chosen sensorless control method is not suitable for high speeds.

10. Conclusion

Utilising the flux/current method to obtain sensorless position estimation on the test setup yielded reasonable results. An error in position of 3° was obtained, which is not feasible in the USAC application. However, it was possible to obtain a rotor speed of 1562 rpm, when given a reference of 1560 rpm. It is also concluded that using the flux/current control method, the rotor speed should not exceed 2500 rpm, since this would cause insufficient number of samples during one cycle of the evaluated flux linkage integral. The sensorless position estimation was attainable with some error in the test setup, however, it is not implemented for closed loop control.

Acknowledgement

The authors of this work gratefully acknowledge Lars Skovlund Andersen from Johnson Controls and Sintex for sponsoring the 5th MechMan symposium.

References

[1] T. Miller, Switched reluctance motors and their control. No. ISBN:0198593872, Hillsboro, 1993.

[2] P. O. Rasmussen, "Transverse flux machine with stator made of e-shaped laminates," Dec. 25 2007. US Patent 7,312,549.

[3] K. Kongerslev, R. Jaeger, and S. S. Nielsen, "Analysis and improvement of u-core switched reluctance machine for electric vehicle drivetrain," tech. rep., Aalborg University, 2015.

[4] M.I.T, Rare Earth Elements. http://web.mit.edu/12.000/www/m2016/finalwebsite/elements/ree.html, 2016. Downloadet: 01.03-2017.

[5] A. B. Kjaer, A. D. Krogsdal, E. H. Nielsen, F. M. Nielsen, S. Korsgaard, and S. P. Moeller, "Sensorless control of a hub mounted switched reluctance machine," tech. rep., Aalborg University, 2017.

[6] P. O. Rasmussen, Design and Advanced Control of Switched Reluctance Motors. No. ISBN:87-89179-40-4, Aalborg University, 2002.

[7] A. K. Kaushik Rajashekara and K. Matsuse, Sensorless Control of AC Motor Drives - Speed and Position Sensorless Operation. No. ISBN:0-7803-1046-2 in 1. Edition, IEEE PRESS, 1993.

[8] E. Kreyszig, Advanced Engineering Mathematics. No. ISBN:978-0-471-72897-9 in 9. Edition, John Wiley and Sons, 2006.